catalysts

MDPI

Article

CO_2-SR: Towards a Cyclic CO_2 Storage and Methane-Assisted Regeneration Technology over an Unsupported Trifunctional Ni–Ba–Ce Catalyst

Sofía Essounani-Mérida [1,2], Sergio Molina-Ramírez [1], Daniel Gallego-García [1], Marina Cortés-Reyes [1,2], Concepción Herrera [1,2,*], María Ángeles Larrubia [1,*] and Luis J. Alemany [1,2]

[1] Departamento de Ingeniería Química, Facultad de Ciencias, Campus de Teatinos, Universidad de Málaga, 29071 Málaga, Spain; sofiaess@uma.es (S.E.-M.); smolina@uma.es (S.M.-R.); danielgallego@uma.es (D.G.-G.); marinacr@uma.es (M.C.-R.); luijo@uma.es (L.J.A.)

[2] Instituto Universitario de Materiales y Nanotecnología, IMANA, Campus de Teatinos, Universidad de Málaga, 29071 Málaga, Spain

* Correspondence: concepcionhd@uma.es (C.H.); mavargas@uma.es (M.Á.L.)

Abstract

CO_2 storage–regeneration (CO_2-SR) is investigated as a cyclic strategy for developing an integrated CO_2 capture-and-conversion technology based on coupling CO_2 storage with methane-assisted regeneration. This work explores trifunctional catalysts integrating CO_2 storage, oxygen exchange and CH_4 activation/regeneration. An unsupported NiBaCe (3/1/5) catalyst was studied as a model system and compared with a NiBa (10/1) reference using N_2 physisorption, XRD, XPS, CO_2-TPD, H_2-TPR, transient O_2 pulse experiments and consecutive CO_2/CH_4 cycles at 600 °C. Ce incorporation increased CO_2 uptake and markedly modified the structural and redox properties of NiBa. Predominant fluorite CeO_2, coexisting surface Ce^{3+}/Ce^{4+} species and a readily reducible low-temperature population evidenced an additional redox-active domain. CO_2-TPD showed that Ce promoted the transformation of adsorbed CO_2-derived species to CO at lower temperatures. O_2 pulse experiments revealed distinct oxygen replenishment behavior: NiBa exhibited prolonged O_2 consumption, whereas the reduced population in NiBaCe was replenished over a shorter timescale. Under consecutive CO_2-SR cycles, both catalysts coupled CO_2 storage with CH_4-assisted regeneration, but NiBaCe exhibited a more reproducible cycle response, with smaller cycle-to-cycle variation but lower absolute H_2 and CO yields, together with a modified product distribution. The results support a trifunctional architecture in which Ba-associated domains provide CO_2 storage, CeO_{2-x} and interfacial redox environments extend the oxygen-buffering/exchange network, and Ni-containing sites promote CH_4 activation and regeneration. Ce therefore does not create the oxygen exchange function of NiBa but reorganizes and extends the pre-existing Ni–O–Ba network through a more readily accessible redox domain. Developing CO_2-SR technology thus requires not only optimizing individual functions, but also their effective dynamic coupling within a trifunctional catalyst.

Keywords: CO_2 storage–regeneration; Ni-based catalysts; ceria; oxygen exchange; CO_2 capture and conversion; methane activation; multifunctional catalysts

Check for updates

Academic Editor: Morris D. Argyle

Received: 7 October 2026
Revised: 9 November 2026
Accepted: 14 November 2026
Published: 19 November 2026

Copyright: © 2026 by the authors. Licensee MDPI, Basel, Switzerland. This article is an open access article distributed under the terms and conditions of the Creative Commons Attribution (CC BY) license.

1. Introduction

The increasing concentration of atmospheric carbon dioxide resulting from anthropogenic activities has led to a significant increase in the search for technologies capable

of simultaneously mitigating greenhouse gas emissions and producing valuable chemicals and fuels. Conventional post-combustion capture methods result in the generation of a concentrated CO_2 stream, which is associated with a significant energy cost due to the necessity of regenerating sorbents or solvents. Among the available approaches, integrated CO_2 capture and utilization (ICCU) has emerged as a promising strategy because it consolidates carbon capture and catalytic conversion within a unified process, potentially mitigating energy expenses and enhancing process efficiency [1–4]. This integration is achieved through dual-function materials (DFMs), in which a basic component chemisorbs CO_2 as surface carbonate species while a metallic component activates a reducing agent and converts the stored carbon, thus avoiding the recovery, compression and transport of a purified CO_2 stream between the capture and conversion stages [5,6]. Methane-assisted cyclic CO_2 storage and regeneration (CO_2-SR) represents a promising ICCU concept in which CO_2 is first captured through the formation of carbonate species and subsequently converted during a separate regeneration stage using methane as a reducing agent. In contrast to conventional dry reforming processes that require the simultaneous feeding of CO_2 and CH_4, the cyclic operation of CO_2-SR temporally separates capture and conversion steps, enabling the production of syngas while integrating CO_2 storage functionality into the catalytic material [3,4,7].

The use of CH_4 as the regeneration reactant avoids the need for an external H_2 feed during the CO_2-SR regeneration stage. This feature is particularly attractive when methane is available from renewable or waste-derived sources, including biogas, although the cyclic CO_2-SR configuration requires the CO_2-containing and CH_4-containing streams to be supplied in temporally separated steps [8,9]. A predominant tendency observed in the literature regarding these processes is the combination of Ni with CaO [10,11]. Recent studies have focused on the stabilization of the sorbent against sintering through structural promoters or perovskite-derived architectures [12,13]. Therefore, the development of multifunctional catalysts capable of efficiently performing both tasks is imperative for the successful implementation of this technology.

Nickel-based materials are widely recognized for their high activity in methane activation, whereas barium-containing phases provide effective CO_2 storage sites through the reversible formation of surface carbonate species [14,15]. The reversibility of the storage step is, in fact, a more restrictive requirement than the storage capacity itself. This is due to the fact that the carbonate formed during the capture stage must decompose and react within the temperature window of the regeneration stage. CaO, the most widely employed sorbent, is limited in this respect because $CaCO_3$ remains thermodynamically stable at typical reforming temperatures, and its progressive accumulation over consecutive cycles leads to capacity loss [16,17]. The CO_2-SR approach is based on the principle of NO_x storage-reduction catalysis [18,19], which is then applied to the valorization of greenhouse gases in unsupported materials. In these catalysts, the interaction between Ni and the alkaline-earth component serves as the governing factor for both functions, instead of a metal–support interface. Previous studies on unsupported Ni-Ba multifunctional catalysts have revealed the feasibility of combining these functionalities within a single material for cyclic CO_2 capture and conversion. The extension of the series to Ca, K, and Sr indicated that catalytic performance is not exclusively predicted by CO_2 uptake, as reducibility and oxygen transfer at the Ni-MO interface were also found to be crucial factors [20]. Nevertheless, the deactivation of catalysts, which is associated with limited oxygen mobility, incomplete regeneration, and structural changes under cyclic conditions, remains a challenge that must be addressed to enhance long-term performance [21,22].

Cerium oxide is well known for its exceptional redox properties, derived from the reversible Ce^{4+}/Ce^{3+} transition, and its remarkable oxygen storage and release

capacity [23–26]. The oxygen vacancies associated with this transition are widely regarded as playing a dual role, acting as sites for CO_2 adsorption and activation and, in many ceria-based systems, as pathways contributing to lattice oxygen mobility [27]. In the context of dry reforming, this behavior contributes to enhanced resistance to carbon deposition, as vacancy-derived oxygen gasifies the carbon formed by methane decomposition prior to its accumulation as inactive coke [28,29]. Ceria has been shown to modify the state of the metallic phase, thereby stabilizing smaller Ni particles and altering their reducibility through Ni-CeO_2 interaction [25,30,31]. In the context of chemical-looping dry reforming, where CH_4 and CO_2 are fed in separate stages, Ni/CeO_2 materials operate as oxygen vectors that cycle between reduced and reoxidized states in step with the feed [32]. The incorporation of cerium into multifunctional CO_2 capture and conversion materials may therefore promote oxygen mobility, facilitate carbon removal, improve regeneration efficiency, and enhance catalytic stability during repeated operation. Recent studies on Ni/$CaCeO_x$ and Ni-CaO/CeO_2 dual-function materials further support the relevance of ceria redox chemistry and of the spatial organization of capture and catalytic domains in integrated CO_2 capture and methane reforming [33,34]. Although these potential advantages are promising, the specific role of cerium in unsupported Ni-Ba-based materials operating under cyclic CO_2-SR conditions requires further elaboration.

In this study, an unsupported trimetallic Ni-Ba-Ce multifunctional catalyst (3/1/5, expressed in atomic ratio) was synthesized and evaluated for the CO_2-SR process. Its performance was compared with the previously developed bimetallic NiBa catalyst (10/1, expressed in atomic ratio) [20,21] to assess how the Ni-Ba-Ce formulation differs from the established NiBa reference in CO_2 storage, syngas production, and cyclic response. Because the two formulations differ in overall metal ratios as well as in the presence of Ce, the comparison is not intended to isolate a composition-independent cerium effect. By combining a physicochemical characterization with the evaluation of the cyclic catalytic response, this study relates the redox behavior and oxygen transfer properties of the material to its performance as a multifunctional catalyst, contributing to the design of more efficient materials for integrated cyclic CO_2 capture and utilization technologies.

2. Results and Discussion

The textural properties of the calcined NiBa 10/1 and NiBaCe 3/1/5 multifunctional catalysts are summarized in Table 1. The NiBaCe formulation exhibits a substantially different textural response from the NiBa: the specific surface area increases from 55 to 71 $m^2 \cdot g^{-1}$, the pore volume from 0.10 to 0.18 $cm^3 \cdot g^{-1}$, and the average pore diameter from 75.2 to 101.9 Å. Both catalysts retain the mesoporous character and relatively high surface areas characteristic of these unsupported formulations, in which colloidal silica is incorporated during synthesis as a nucleating agent and textural promoter [20]. The higher surface area and pore volume of NiBaCe indicate a more open porous structure.

Table 1. This BET surface area (A_{BET}), pore volume (V_p), and average pore diameter (d_p) of the calcined NiBa and NiBaCe catalysts, determined by N_2 physisorption.

	A_{BET} $m^2 \cdot g^{-1}$	V_p $cm^3 \cdot g^{-1}$	d_p Å
NiBa	55	0.10	75.21
NiBaCe	71	0.18	101.94

Figure 1 presents the X-ray diffraction patterns of the two calcined catalysts. The NiBa sample exhibits sharp and intense diffraction peaks corresponding to cubic NiO (2θ = 37.3, 43.3, 62.9, 75.4, and 79.4°), together with a weak reflection at 24.0° assigned to

orthorhombic $BaCO_3$ and a low-intensity signal at 26.0° attributed to SiO_2 originating from the colloidal silica used in the preparation. The narrow NiO reflections correspond to an average crystallite size of 250.4 Å, consistent with well-developed nickel oxide domains. The weak $BaCO_3$ reflection demonstrates that only a minor fraction of Ba is detected as a crystalline carbonate phase by XRD; the diffraction data alone do not establish the form or spatial distribution of the remaining Ba species. In contrast, the diffractogram of NiBaCe is dominated by fluorite-type CeO_2 (2θ = 28.54, 33.07, 47.47, 56.3, 59.0, 69.2, 76.7 and 79.0°), with a crystallite size of 97.5 Å. No separate NiO or Ba-containing crystalline phases are resolved, this observation is consistent with Ni- and Ba-containing species highly dispersed, poorly crystalline and/or amorphous environments.

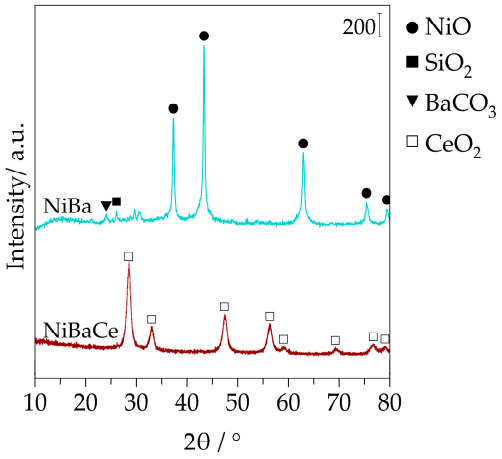


Figure 1. X-ray diffraction patterns of calcined NiBa and NiBaCe catalysts.

Table 2 resumes the crystallite sizes, and the unit-cell parameters of the phases detected in DRX. Cell parameters are not reported for $BaCO_3$, this phase corresponds to a single weak reflection at about 24°, its estimated weight fraction is only 0.73%, and its refined cell showed deviations of +1.59% in c and +1.21% in cell volume relative to the reference pattern (ICDD 04-016-3101), indicating that it is not reliably refinable from these data. For NiO, the reference pattern (ICDD 04-016-1090) is indexed on a doubled cell (a = 8.3578 Å, $Ni_{32}O_{32}$); the value reported here, a = 4.1789 Å, corresponds to the standard rock-salt NiO unit cell. The refinement of CeO_2 against the reference pattern (ICDD 01-086-4481) converged to a = 5.4128 Å with a Bragg R-factor of 3.55%. This outcome confirms that, in contrast to $BaCO_3$ and NiO, this phase is completely refinable from the available data.

Table 2. Crystallite size and unit-cell parameters of the phases identified by X-ray diffraction in the calcined NiBa and NiBaCe catalysts, obtained by Rietveld refinement.

		Crystallite Size Å	A Å	b Å	c Å	α °	β °	γ °	Structure -
NiBa	NiO	250	4.1789	4.1789	4.1789	90	90	90	Cubic
NiBaCe	CeO_2	98	5.4128	5.4128	5.4128	90	90	90	Cubic

The diffraction patterns therefore show a marked difference in the crystalline organization of the two formulations rather than the simple appearance of an additional crystalline oxide. NiBa is dominated by well-developed NiO crystallites, whereas CeO_2 is the only crystalline phase resolved in NiBaCe and no separate NiO- or Ba-containing crystalline phases are detected.

This structural reorganization is particularly relevant to the multifunctional nature required for the CO_2-SR process. The reference NiBa formulation combines Ba-containing

domains involved in CO_2 uptake and storage with Ni-containing domains required for CH_4 activation during regeneration. Previous studies on this catalyst series have associated the coupling between these functions with interfacial Ni–O–Ba environments [20,21]. The incorporation of Ce introduces an additional redox-active component with the potential to extend this oxygen exchange network through the reversible Ce^{4+}/Ce^{3+} couple and the associated formation and act as an oxygen buffer and transfer mediator [24,26]. Ceria-based oxygen exchange has also been associated with improved regeneration and resistance to carbon deposition in methane reforming environments [28,32]. From a structural standpoint, NiBaCe can therefore be viewed as a material containing three potentially interacting domains: Ba-rich CO_2 storage domains, Ni-rich CH_4-activation domains, and Ce-containing redox domains.

X-ray photoelectron spectroscopy was used to examine the surface chemical environments of Ni, Ba and Ce, binding energies and species assignments for the Ni $2p_{3/2}$ and Ba $3d_{5/2}$ regions are summarized in Table 3. For NiBaCe, the XPS-derived surface atomic ratio is close to the nominal Ni/Ba/Ce formulation. Converting the XPS-derived surface atomic composition to a mass basis gives approximately 47 wt.% Ni for NiBa and approximately 11 wt.% Ni for NiBaCe; as these are unsupported bulk materials rather than catalysts dispersed on a support, these values are presented as XPS-derived surface mass fractions rather than as a conventional support-normalized loading figure.

Table 3. Binding energies and species assignments for the Ni $2p_{3/2}$ and Ba $3d_{5/2}$ regions of the calcined NiBa and NiBaCe catalysts.

Catalyst	Ni $2p_{3/2}$		Ba $3d_{5/2}$	
	B. E. (eV.)	Species	B. E. (eV.)	Species
NiBa	855.1	Ni^{2+}	777.7	BaO
	861.1	Ni^{2+} sat.	779.9	$BaO.CO_2$ BaO.NiO
NiBaCe	855.3	Ni^{2+}	779.9	$BaO.CO_2$ BaO.NiO
	860.8	Ni^{2+} sat.		

The Ni $2p_{3/2}$ spectra of both catalysts show a main peak at 855.1–855.3 eV accompanied by the shake-up satellite at 860.8–861.1 eV, consistent with Ni^{2+} in NiO or Ni species interacting with Ba-containing phases, in agreement with previous assignments for this catalyst series [20,21]. The oxidation state of nickel is therefore essentially unchanged upon Ce incorporation, although its structural environment is markedly different. XRD resolves crystalline NiO in NiBa but no separate NiO phase in NiBaCe.

For NiBa, the Ba $3d_{5/2}$ region resolves two components at 777.70 and 779.88 eV. The lower-binding-energy contribution is assigned to BaO, whereas the component at 779.88 eV may contain overlapping contributions from surface-carbonated Ba and Ba–Ni interfacial species, which cannot be reliably distinguished solely from their binding energies. A similar overlap has previously been reported for the Ba $4d_{5/2}$ region of this catalyst series [20,21]. The weak $BaCO_3$ reflection detected by XRD indicates that only a minor fraction of Ba forms a crystalline carbonate phase, supporting the presence of a substantial fraction of Ba as highly dispersed surface and interfacial species.

In NiBaCe, only the higher-binding-energy Ba $3d_{5/2}$ contribution at 779.93 eV is resolved, with no distinguishable BaO component analogous to that observed for NiBa. Together with the absence of a resolved crystalline Ba-containing phase by XRD, this result is consistent with a different Ba surface environment in the Ni-Ba-Ce formulation. The available XPS and XRD data support the presence of non-bulk-like Ba environments but do not uniquely determine whether these correspond to highly dispersed, amorphous or specific interfacial species.

The O 1s region of both catalysts was resolved using the same three-component model previously applied to this catalyst series [21]: a low-binding-energy contribution (O_I, 529–530 eV) assigned predominantly to lattice oxygen in metal–oxygen bonds, an intermediate contribution (O_{II}, 531–532 eV) associated with surface hydroxyls and chemisorbed/defect-related oxygen species, and a higher-binding-energy contribution (O_{III}, ~533 eV) associated with physisorbed water and carbonate-type species (Figure 2a,b). NiBa exhibits OI = 49.5% and O_{II+III} = 50.5%, whereas NiBaCe gives O_I = 53.1% and O_{II+III} = 46.9%. Thus, Ce incorporation does not produce an increase in the overall non-lattice O 1s contribution. Importantly, the O_{II} contribution should not be interpreted as a direct measurement of oxygen-vacancy concentration. Ex situ XPS necessarily probes a hydroxylated and partially carbonated surface, and signals in the 531–532 eV region generally contain substantial contributions from hydroxyl and chemisorbed oxygen species [35,36]. Consequently, O 1s alone cannot establish the concentration or accessibility of oxygen vacancies relevant to the CO_2-SR cycle.

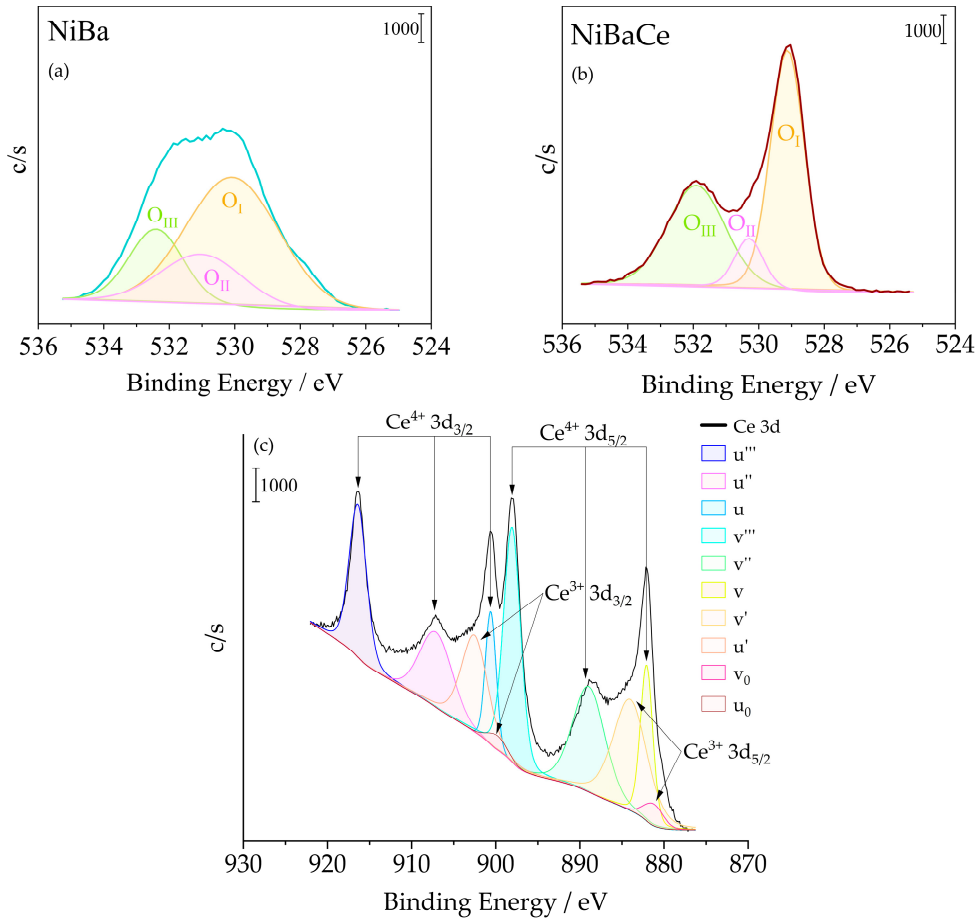


Figure 2. Deconvoluted O 1s XPS spectra of the calcined (**a**) NiBa and (**b**) NiBaCe catalyst. (**c**) The deconvoluted Ce 3d XPS spectrum of the calcined NiBaCe catalyst.

The Ce 3d region was fitted with the ten-component model established by Romeo et al. [37] and discussed by Paparazzo [38], comprising the characteristic Ce^{4+} and Ce^{3+} spin–orbit doublets (Figure 2c). The fitted areas indicate approximately 31.5% Ce^{3+} and 68.5% Ce^{4+} at the surface. Although the exact Ce^{3+} fraction should be treated cautiously because of the weak intensity and strong overlap of some Ce^{3+} components, the value is consistent with a substantial population of reduced surface Ce centers and is comparable to the surface enrichment reported for Ni-doped CeO_2 [39].

Increased surface Ce^{3+} fractions are generally considered indicative of a ceria lattice capable of participating in oxygen exchange [40,41]. However, the static Ce^{3+} fraction does not by itself demonstrate either oxygen mobility or oxygen transfer between the Ba- and Ni-containing domains. Rather, the XPS results establish the presence of a redox-active Ce^{3+}/Ce^{4+} surface environment that could provide an additional oxygen-buffering function.

The combined results of XRD and XPS therefore establish the structural basis for a three-domain description of NiBaCe: dispersed Ba-containing species associated with CO_2 storage, Ni-containing species associated with CH_4 activation, and a Ce^{3+}/Ce^{4+}-containing ceria domain potentially capable of oxygen buffering and exchange. Despite providing valuable insight into the surface oxygen chemistry, these results do not directly reveal the direction, rate, or magnitude of oxygen transfer under CO_2-SR conditions. Consequently, the central question is whether the incorporation of Ce modifies the availability and transfer dynamics of oxygen species responsible for linking CO_2 capture and CH_4-assisted regeneration. This aspect is explored in the following sections through CO_2 activation measurements, H_2-TPR characterization, transient O_2 reoxidation studies, and cyclic CO_2/CH_4 experiments.

Prior to the temperature-programmed desorption experiment, the amount of CO_2 retained during the adsorption step was quantified as 0.198 and 0.332 mmol CO_2 $gcat^{-1}$ for NiBa and NiBaCe, respectively, corresponding to a 68% higher gravimetric CO_2 uptake for NiBaCe. This increase is partly associated with the larger BET surface area of NiBaCe. Indeed, when the CO_2 uptake is normalized to the specific surface area, values of 3.6 and 4.7 μmol CO_2 m^{-2} are obtained for NiBa and NiBaCe, respectively, corresponding to an increase of approximately 30%. The comparison between the gravimetric and surface-area-normalized uptakes therefore indicates that the enhanced CO_2 retention of NiBaCe cannot simply be attributed to its larger surface area. Although the increase becomes less pronounced after BET normalization, the higher CO_2 uptake per unit surface area suggests differences in the abundance, accessibility and/or nature of the surface sites involved in CO_2 retention. After the adsorption step, the temperature was increased until 800 °C and the resulting CO_2 and CO evolution profiles as a function of temperature are shown in Figure 3. The integration of the CO_2 desorption profiles in Figure 3a yielded 6.4 and 10.5 μmol CO_2 $gcat^{-1}$ for NiBa and NiBaCe, respectively. These values correspond exclusively to molecular CO_2 evolved during the temperature ramp and are therefore used to compare the behavior of the two catalysts. The substantially larger amount of CO_2 retained during the adsorption step relative to the CO_2 subsequently desorbed as a molecular species indicates that most of the retained CO_2-derived species are not released as molecular CO_2 under these conditions, consistent with the concurrent formation of CO described below.

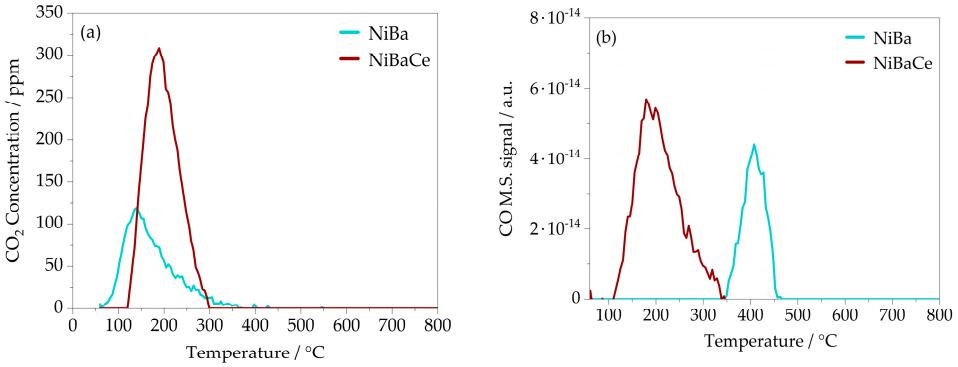


Figure 3. CO_2-TPD profiles of the calcined NiBa and NiBaCe catalysts: (**a**) CO_2 concentration and (**b**) CO signal recorded by mass spectrometry.

The CO_2 desorption profiles (Figure 3a) also reveal a change in the nature of the stored species. NiBaCe exhibits a more intense and narrower desorption feature centered at approximately 189 °C, returning to the baseline at around 300 °C. In contrast, NiBa shows a broader response extending to approximately 350 °C. According to the classification previously established for this catalyst series, CO_2 desorption below 300 °C is mainly associated with weak basic sites, whereas more strongly retained species desorb at higher temperatures. The Ce-containing catalyst therefore combines a larger CO_2 uptake with a distribution shifted towards more weakly bound, and potentially more readily regenerated, CO_2-derived species.

A more significant difference emerges from the CO profiles (Figure 3b). NiBa produces a CO feature centered at approximately 400 °C, whereas CO evolution over NiBaCe occurs predominantly between 150 and 300 °C. Unlike molecular CO_2 desorption, CO formation under inert flow requires transformation of the adsorbed CO_2-derived species through a reduction pathway. In this unsupported catalyst series, such behavior has previously been associated with the coexistence of NiO and reduced Ni species, which enables the conversion of adsorbed CO_2 to CO [20]. The shift in CO evolution by more than 100 °C towards lower temperature in NiBaCe therefore indicates that the stored CO_2-derived species can access a redox pathway considerably more readily when Ce is present.

Overall, the NiBaCe catalyst differs from NiBa in two properties directly relevant to the CO_2-SR cycle: it retains a larger amount of CO_2, predominantly as relatively weakly bound species, and requires a substantially lower temperature for their conversion to CO. The former defines the storage function, whereas the latter provides the first functional evidence that the redox accessibility of the stored CO_2-derived species differs between the two catalysts. Whether this enhanced redox accessibility is associated with a more readily exchangeable oxygen population is examined next by H_2-TPR and transient O_2 reoxidation experiments.

The H_2-TPR profiles of NiBa and NiBaCe are presented in Figure 4 and provide information on the reducibility of the oxide species and the interactions established within these unsupported catalysts. The NiBa catalyst exhibits a broad reduction region dominated by a high-temperature maximum at approximately 734 °C. A weak and broad feature is also observed around 225 °C, accounting for less than 2% of the recorded signal, followed by a minimum at approximately 340 °C before the onset of the main reduction envelope. Previous deconvolution of the NiBa profile resolved two contributions centered at 642 and 737 °C, assigned, respectively, to Ni species associated with more H_2-accessible Ni–O–Ba interfacial environments and to Ni–O–Ni environments in the proximity of Ba-containing domains [21]. The predominance of reduction at high temperature is consistent with the well-developed NiO domains identified by XRD (ca. 250 Å) and indicates that most of the reducible Ni-containing species in NiBa are comparatively difficult to reduce.

This reduction behavior is markedly different in NiBaCe. In addition to the broad high-temperature reduction envelope, NiBaCe exhibits a distinct contribution beginning at substantially lower temperature, with a maximum at approximately 318 °C and a shoulder extending towards 360 °C. This feature falls within the low-temperature reduction region reported for Ni/CeO_2 systems. Luisetto et al. [42] described a β reduction region between approximately 300 and 550 °C associated with NiO species interacting with ceria, together with a lower-temperature α contribution below 300 °C assigned to more readily reducible Ni–O–Ce environments. The low-temperature contribution observed for NiBaCe is therefore consistent with the formation of Ni–Ce interfacial environments and/or Ce-associated oxygen species that become reducible at considerably lower temperature than the dominant Ni-containing species in NiBa. This assignment should nevertheless be regarded as indicative rather than exclusive, since H_2-TPR alone cannot unambiguously distinguish between

reduction in Ni species interacting with ceria and reduction in labile oxygen associated with the Ce-containing phase.

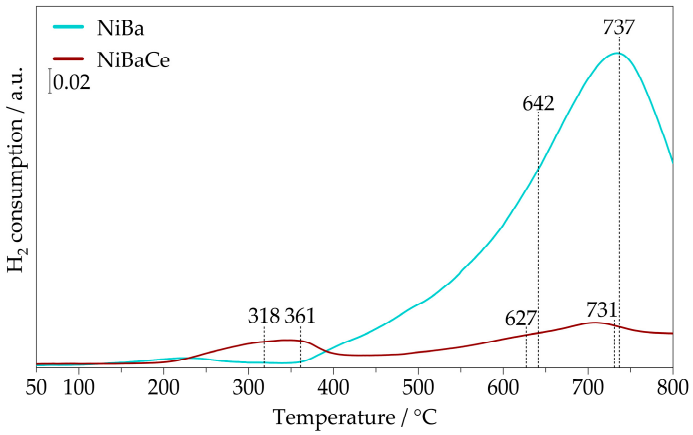


Figure 4. H_2-TPR profiles of the calcined NiBa and NiBaCe catalysts.

At higher temperature, the NiBaCe profile develops a broad reduction envelope that extends towards the upper experimental limit of 800 °C without fully returning to the baseline. This region is intrinsically complex because a reduction in Ni-containing species overlaps with that of ceria. Pure CeO_2 undergoes reduction over different temperature ranges associated with surface and bulk oxygen, and its high-temperature bulk reduction can shift towards lower temperature in the presence of other interacting cations [42,43]. NiO species in unsupported catalysts of this series are reduced over a comparable temperature interval [20]. In addition, as previously reported for the bimetallic catalyst series, decomposition of residual carbonate species may contribute to H_2 consumption within the same high-temperature region [20]. Consequently, the high-temperature envelope of NiBaCe most likely contains overlapping contributions from Ni- and Ce-containing reducible species, together with a possible contribution from carbonate decomposition, and cannot be assigned unambiguously to a single oxide environment.

The incomplete return of the NiBaCe profile to the baseline at 800 °C also limits the quantitative interpretation of its mathematical deconvolution. Because the descending part of the high-temperature reduction envelope is not fully contained within the experimental temperature window, the position, width and relative areas of overlapping high-temperature components cannot be determined independently with sufficient confidence. Although an exploratory deconvolution can reproduce the overall profile, the fitted high-temperature components are therefore not used here for quantitative analysis or for assignment to individual chemical species. In particular, relative contributions derived from the total fitted area are not considered, since the high-temperature area is affected by truncation at the upper experimental limit.

In contrast, the low-temperature contribution centered at approximately 318 °C, with a shoulder extending towards 360 °C, is fully contained within the experimental temperature range and therefore represents a robust difference between the two catalysts. Accordingly, the mechanistically relevant result of the H_2-TPR experiment is not the number or relative area of fitted high-temperature components, but the clear emergence of a low-temperature reducible population upon Ce incorporation. Although its precise chemical origin cannot be established from H_2-TPR alone, its temperature range and the reported behavior of Ni/CeO_2 systems are consistent with Ni–Ce interfacial interactions and Ce-assisted reduction [42].

To summarize, the H_2-TPR results indicate that the reduction behavior of NiBaCe differs substantially from that of NiBa, with the NiBaCe catalyst exhibiting a population

of species that becomes reducible at significantly lower temperature. This observation is consistent with the lower-temperature CO evolution observed during CO_2-TPD and reinforces the conclusion that Ce increases the redox accessibility of the NiBa system. Importantly, enhanced reducibility does not necessarily imply faster oxygen transfer. H_2-TPR establishes the accessibility of reducible species under a temperature-programmed reducing atmosphere but does not directly probe how rapidly oxygen can be exchanged and replenished under cyclic conditions. The transient O_2 reoxidation experiments discussed below therefore provide complementary information to determine whether the enhanced redox accessibility of NiBaCe is accompanied by a more dynamic oxygen exchange behavior.

These results indicate that the role of Ce extends beyond the incorporation of an additional oxide component. The structural reorganization induced by Ce, the presence of the Ce^{3+}/Ce^{4+} redox couple, and particularly the emergence of a low-temperature reducible population supports the presence of a more readily accessible redox domain within the NiBaCe catalyst. This domain could provide an additional route for oxygen exchange between the Ba-containing CO_2 storage environments and the Ni-containing sites involved in methane-assisted regeneration, complementing the direct Ni–O–Ba interfacial exchange already proposed for the reference NiBa catalyst. Accordingly, the lower-temperature reduction observed by H_2-TPR and the shift in CO formation towards lower temperature during CO_2-TPD are consistent with improved redox accessibility of the stored CO_2-derived species when Ce is present. It should also be stressed, following Feng et al., that a larger oxygen-defect population is not by itself sufficient to improve cyclic performance. Optimum behavior is expected to depend on the balance between accessible Ni sites, Ce-associated oxygen buffering and the degree of interaction between the Ba-, Ni- and Ce-containing domains, rather than maximizing any of these properties independently [44].

To examine the accessibility and replenishment of oxygen-deficient sites more directly, transient O_2 pulse experiments were performed over previously reduced NiBa and NiBaCe catalysts at 600 °C (Figure 5), following the transient pulse approach previously applied to this catalyst series [45]. During the initial pulses, incoming O_2 can be consumed through the reoxidation of oxygen-deficient sites, as well as through the oxidation of residual reduced species remaining after the reduction pretreatment. The simultaneous evolution of CO, CO_2 and H_2O indicates that part of the supplied oxygen also reacts with residual carbon- and hydrogen-containing species. As the available oxygen-deficient sites are progressively reoxidized, O_2 consumption decreases and the gas-phase O_2 response increases until a stable plateau is reached, indicating that the oxygen uptake capacity available under these experimental conditions has been approached.

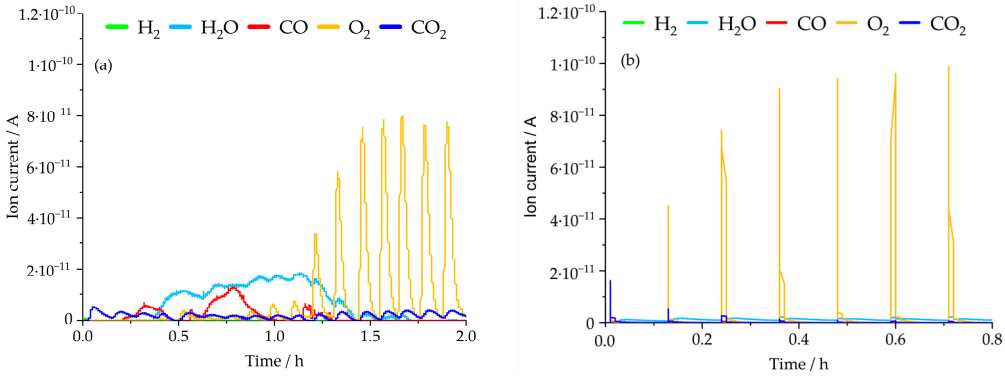


Figure 5. Mass spectrometry response of (**a**) NiBa and (**b**) NiBaCe to successive 250 µL O_2 pulses over the previously reduced catalysts at 600 °C. Each O_2 pulse was followed by a He purge, and the sequence was continued until complete O_2 breakthrough was reached.

The two catalysts display markedly different transient responses. For NiBa (Figure 5a), O_2 uptake persists over an extended period: CO, CO_2 and H_2O remain detectable for approximately 1.2 h, while the O_2 response increases gradually and requires several additional pulses to approach a stable plateau. In contrast, for NiBaCe (Figure 5b), a fraction of the injected O_2 is already detected from the second pulse and the response approaches its plateau after approximately five pulses, i.e., in less than 0.5 h, with only minor concurrent formation of CO, CO_2 and H_2O. These contrasting profiles highlight differences in both the extent and timescale of the reoxidation response of the two catalysts. The prolonged O_2 consumption observed for NiBa is consistent with a larger accessible O_2 uptake capacity under the experimental conditions, which is progressively replenished over a comparatively long period. NiBaCe, in contrast, shows a lower overall O_2 consumption and approaches its plateau considerably faster, indicating a more limited O_2 uptake capacity but a shorter reoxidation timescale. Integration of the transient O_2 uptake profiles gives a total O_2 consumption of approximately 1470 and 452 μmol g^{-1} for NiBa and NiBaCe, respectively. This behavior is consistent with the structural and redox features identified above: NiBa contains large crystalline NiO domains and shows predominantly high-temperature reduction features, whereas NiBaCe lacks a separately detectable crystalline NiO phase and exhibits a distinct low-temperature reducible population in the Ce-containing formulation. Overall, the transient experiments show that the two catalyst formulations differ not only in the amount of oxygen consumed during reoxidation, but also in the timescale over which this process occurs. However, the faster O_2 response of NiBaCe should not by itself be interpreted as direct evidence of higher intrinsic oxygen mobility, since the transient response also depends on the total number and nature of the sites available for oxygen uptake.

This difference can be quantified using the same transient descriptors previously applied to this catalyst series [45]. The breakthrough time (t_b), defined as the time at which O_2 is first detected in the outlet stream, decreases from approximately 1.0 h for NiBa to <0.06 h for NiBaCe. Similarly, the time required to reach half of the plateau O_2 response ($t_1/_2$) decreases from 1.2 h for NiBa to 0.15 h for NiBaCe (Figure 5). These values quantitatively confirm the markedly different timescales of the reoxidation response of the two catalysts, with O_2 appearing in the outlet and approaching its plateau considerably earlier for NiBaCe. The substantially shorter tb and $t_{1/2}$ values of NiBaCe are consistent with a more rapidly accessible and replenished oxygen population in the Ce-containing catalyst. Thus, whereas H_2-TPR shows enhanced redox accessibility for NiBaCe relative to NiBa, the transient O_2 experiments provide complementary kinetic evidence that the oxygen-deficient population in NiBaCe can be replenished over a substantially shorter timescale. These observations support the participation of the Ce-containing domain in a more dynamic oxygen exchange network coupling CO_2 storage and methane-assisted regeneration.

The cyclic CO_2-SR experiments were performed to directly evaluate their ability to repeatedly store CO2 and subsequently regenerate the catalyst through reaction with CH_4.

The outlet concentration profiles recorded during ten consecutive cycles are shown in Figure 6 for NiBa (Figure 6a) and NiBaCe (Figure 6b), while the corresponding CO_2/CO and H_2/CO_x ratios are compared in Figure 6c.

For both catalysts, each CO_2 storage step is accompanied by a rapid increase in the outlet CO_2 concentration, whereas switching to CH_4 results in the simultaneous evolution of H_2 and CO. This response demonstrates the cyclic coupling between CO_2 storage and CH_4-assisted regeneration of the species accumulated during the preceding storage step. Integration of the transient profiles provides a quantitative description of the evolution of the system during cycling and reveals clear differences between the two catalysts.

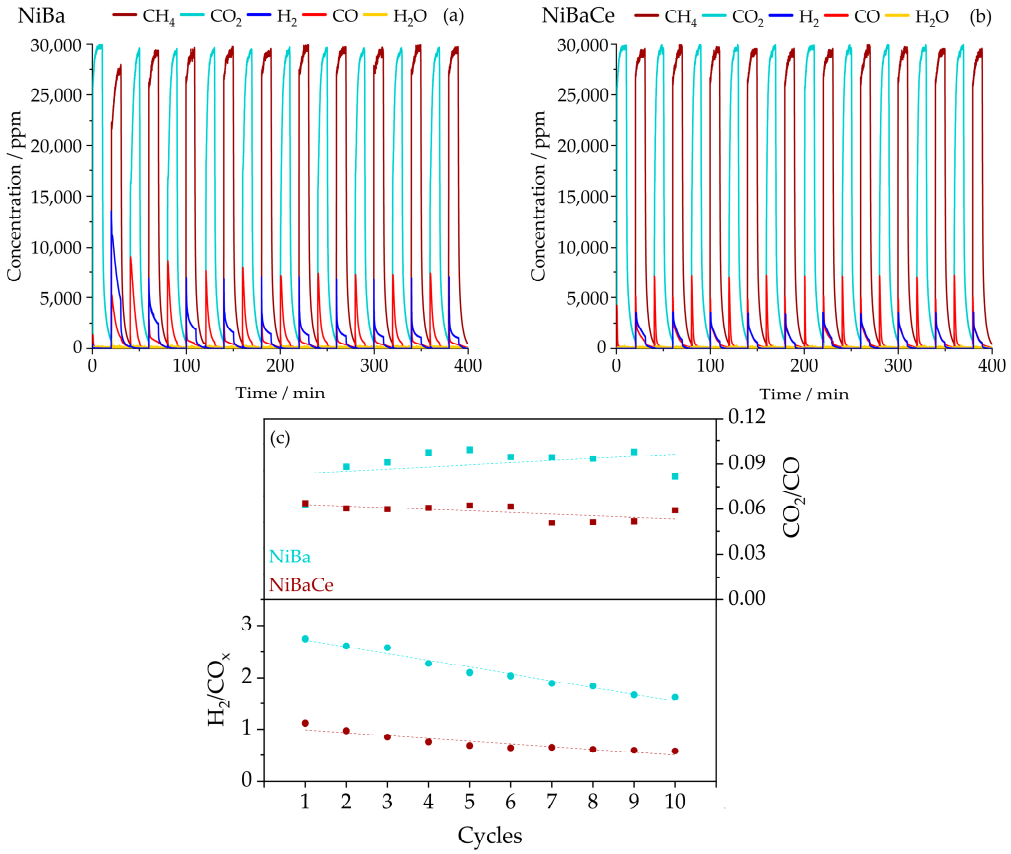


Figure 6. Outlet concentration profiles of CH_4, CO_2, H_2, CO and H_2O during ten consecutive CO_2-SR cycles over (**a**) NiBa and (**b**) NiBaCe at 600 °C, using alternating CO_2 and CH_4 pulses (30,000 ppm each, He balance) separated by He purge steps; (**c**) evolution of the CO_2/CO and H_2/CO_x ratios over the ten cycles.

For NiBa, the amount of H_2 evolved during CH_4-assisted regeneration decreases from approximately 3.94 to 0.74 mmol g^{-1}, while the amount of CO decreases from 1.35 to 0.42 mmol g^{-1}. The corresponding amount of CO_2 released or remaining unretained during the storage/regeneration sequence changes from 0.08 to 0.03 mmol g^{-1}. The largest variation occurs between the first and subsequent cycles, particularly for H_2, indicating a pronounced first-cycle transient. Thereafter, the amounts of the main gaseous products progressively approach a quasi-stationary cyclic response. A similar, although less pronounced, evolution is observed for CO. NiBaCe exhibits a markedly different behavior. The integrated amounts of H_2 and CO generated during the first regeneration step are already close to those measured in the subsequent cycles. Over the ten cycles, H_2 evolution varies from 0.99 to 0.56 mmol g^{-1}, whereas CO evolution changes only from 0.84 to 0.80 mmol g^{-1}. Thus, NiBaCe displays a substantially smaller cycle-to-cycle variation and reaches its cyclic state more rapidly than NiBa, which had not yet reached a fully stationary response within the ten cycles studied. Nevertheless, this faster settling comes with lower absolute H_2 and CO productivity than NiBa. This difference in absolute productivity is consistent with the substantially lower Ni content of NiBaCe (approximately 11 wt.%) relative to NiBa (approximately 47 wt.%): when H_2 production is normalized to the Ni content of each catalyst, NiBaCe yields more H_2 per mol of Ni than NiBa at both the first and the tenth cycle, indicating that the lower absolute output of NiBaCe reflects its lower Ni loading rather than a lower intrinsic activity of its Ni sites, with this difference increasing over cycling.

The evolution of carbon-containing products also provides information on the redistribution of stored carbon during regeneration. Comparison of the integrated CO_2 and

CO amounts shows that NiBa maintains a larger relative contribution of CO_2, whereas NiBaCe exhibits a larger contribution of CO within the carbon-containing products. This difference is reflected in the CO_2/CO ratio shown in Figure 6c, which remains higher for NiBa than for NiBaCe throughout the ten cycles. Similarly, NiBa exhibits a higher H_2/CO_x ratio, decreasing from approximately 2.7 in the first cycle to 1.6 in the tenth cycle, whereas NiBaCe shows a lower H_2/CO_x ratio and a substantially smaller variation over the same period. The progressive evolution of these ratios, in combination with the integrated H_2, CO and CO_2 amounts, indicates that the relative contributions of the reactions occurring during CH_4-assisted regeneration change during repeated cycling. Such changes may involve variations in the amount and reactivity of carbonate and carbonaceous species and in the availability of oxygen-containing surface or interfacial species, as previously observed for this catalyst series [21,22]. The lower and more stable ratios observed for NiBaCe therefore indicate a different balance between the reactions involved in regeneration.

These product ratios provide a carbon/hydrogen product balance during the cyclic experiment but should not be interpreted as direct measurements of oxygen storage capacity or oxygen mobility. Instead, they describe how stored CO_2-derived species are redistributed into gaseous products during CH_4-assisted regeneration and provide the experimental basis for discussing the sequence of functions involved in the cycle. The cyclic behavior can be related to the preceding characterization results. CO_2-TPD showed that NiBaCe retains more CO_2 and converts stored CO_2-derived species to CO at lower temperature than NiBa; H_2-TPR revealed the emergence of a low-temperature reducible population; and the transient O_2 experiments showed that the oxygen-deficient population generated in NiBaCe is replenished over a substantially shorter timescale. Figure 6 therefore provides complementary information on how these individual properties are expressed when CO_2 storage and CH_4-assisted regeneration are repeatedly coupled in the same catalyst.

These results support a mechanistic description of the cycle based on three coupled functions: (i) CO_2 capture and formation of stored carbonate-like species; (ii) exchange/transfer of oxygen associated with interfacial oxide environments; and (iii) CH_4 activation and regeneration of the storage/redox functions with simultaneous formation of H_2 and CO/CO_2. In the reference NiBa catalyst, Ba-containing domains provide the principal CO_2 storage function, while Ni-containing sites activate CH_4 during regeneration. The pronounced first-cycle transient observed for NiBa indicates that the initial catalyst state differs from that subsequently established under repeated CO_2/CH_4 cycling. However, these experiments do not allow this evolution to be assigned exclusively to a specific oxygen transfer step. These functions are coupled through dynamically exchangeable Ni–O–Ba interfacial environments, previously identified as relevant descriptors within this unsupported Ni–M catalyst series [20,21,45].

Ce incorporation introduces an additional redox-active domain into the storage–regeneration architecture. The Ce^{3+}/Ce^{4+} environment identified by XPS, the lower-temperature conversion of stored CO_2-derived species during CO_2-TPD, the low-temperature reducible population detected by H_2-TPR, and the shorter characteristic re-oxidation times observed during the O_2 pulse experiments are consistent with a more readily accessible and dynamic redox environment in NiBaCe. Within this framework, non-stoichiometric CeO_{2-x} may contribute to oxygen buffering and exchange between Ba-containing storage environments and Ni-containing regeneration sites, in addition to the direct Ni–O–Ba exchange previously identified in NiBa.

In NiBaCe, the Ce-containing environment provides an additional redox contribution to this architecture rather than replacing the functions associated with Ba and Ni. The

mechanistic distinction between the two catalysts can therefore be represented schematically as follows:

$$\text{NiBa} \qquad \text{Ba–carbonate} \rightleftarrows \text{Ni–O–Ba} \rightleftarrows \text{Ni–CH}_x$$

$$\text{NiBaCe} \qquad \text{Ba–carbonate} \rightleftarrows [\text{Ba–O–Ce/CeO}_{2-x}\text{/Ce–O–Ni}] \rightleftarrows \text{Ni–CH}_x$$

These schemes represent functional relationships rather than unique sequences of elementary steps. Direct Ni–O–Ba exchange may remain operative in NiBaCe, while Ni–O–Ce and Ba–O–Ce interfacial environments may provide additional pathways for oxygen redistribution between the storage and regeneration functions. The smaller cycle-to-cycle variation observed for NiBaCe over the ten cycles studied is consistent with this modified redox environment, although it does not establish a specific oxygen transfer pathway or demonstrate long-term stability.

Accordingly, the role of Ce cannot simply be described in terms of increased CO_2 uptake, reducibility or oxygen-vacancy concentration. The cyclic behavior is consistent with a balance and connectivity between the three functional domains: Ba-containing environments determine CO_2 storage, Ce-containing environments contribute to oxygen buffering and exchange, and Ni-containing sites govern CH_4 activation and regeneration. This interpretation is consistent with the concept that oxygen vacancies alone are insufficient to determine catalytic performance and that the accessibility and connectivity of the redox network are equally important [44]. Thus, rather than creating a new oxygen exchange function, Ce is proposed to reorganize and extend an existing Ni-O-Ba exchange network by introducing an additional, more readily accessible redox domain.

Based on the combined CO_2-TPD, H_2-TPR, transient O_2 pulse and cyclic CO_2-SR results, catalyst operation can be represented by the simplified functional scheme shown in Figure 7. The scheme is deliberately formulated in terms of surface/storage species and exchangeable oxygen rather than as a set of elementary defect-chemical reactions. The cyclic evolution of CO_2, CO and H_2, together with the different transient responses of NiBa and NiBaCe, is consistent with a sequence of coupled CO_2 storage and CH_4-assisted regeneration steps. CO_2 is first retained as surface CO_2-derived species, predominantly within Ba-associated basic domains. Exchangeable oxygen is subsequently redistributed through the interfacial redox network, which in NiBa involves Ni–O–Ba environments and, after Ce incorporation, may additionally involve CeO_{2-x} and Ni–O–Ce/Ba–O–Ce environments. During regeneration, CH_4 activation at Ni-containing sites consumes exchangeable oxygen and stored CO_2-derived species, leading to the formation of H_2 and CO, with CO_2 also evolving depending on the local oxidation state. This process regenerates oxygen-deficient sites for the subsequent CO_2 storage step. Figure 7 therefore provides a functional representation of the cyclic process in terms of three coupled functions: CO_2 storage, interfacial oxygen exchange and CH_4-assisted regeneration.

In this representation, □ denotes an oxygen-deficient site (oxygen vacancy). The equations describe the overall transformations of surface/storage species and exchangeable oxygen within each stage and are not intended to represent individual elementary reaction steps.

CO_2 storage occurs primarily within the basic Ba-containing domains, with $BaO/BaCO_3$ providing the main storage function. The interaction of gaseous CO_2 with basic surface oxygen species is represented by the formation of surface carbonate species:

$$CO_2\ (g) + O^{2-}\ (surf) \rightleftharpoons {CO_3}^{2-}\ (surf)$$

while the participation of an oxygen-deficient site in the storage process is represented as follows:

$$CO_2\ (g) + \square + O^{2-}\ (surf) \rightleftharpoons {CO_3}^{2-}\ (surf)$$

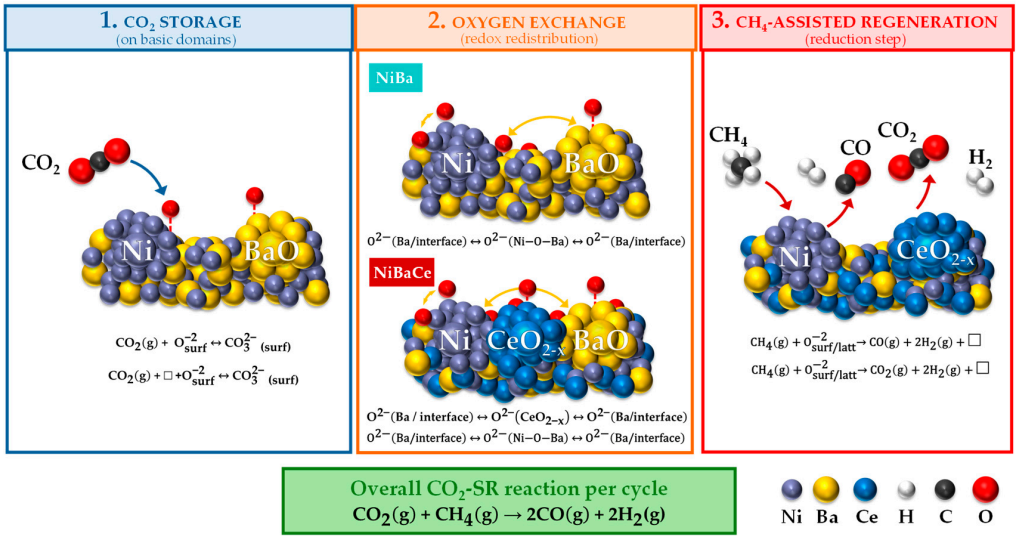


Figure 7. A simplified coupled reaction scheme proposed for the CO_2-SR cycle, shown separately for NiBa (Step 1) and NiBaCe (Step 3), with both catalysts compared in Step 2.

Following CO_2 storage, exchangeable oxygen can be reversibly redistributed through the interfacial redox network. In NiBa, oxygen exchange between the Ba-containing storage environment and the Ni-containing regeneration environment is represented as follows:

$$O^{2-}\ (Ba/interface) \rightleftharpoons O^{2-}\ (Ni–O–Ba) \rightleftharpoons O^{2-}\ (Ni/interface)$$

For NiBaCe, CeO_{2-x} provides an additional oxygen-buffering pathway connecting the Ba-containing storage domains with the Ni-containing activation sites.

$$O^{2-}\ (Ba/interface) \rightleftharpoons O^{2-}\ (CeO_{2-x}) \rightleftharpoons O^{2-}\ (Ni/interface)$$

During CH_4-assisted regeneration, Ni-containing sites provide the main CH_4-activation function, while exchangeable surface/lattice oxygen is consumed. The formation of CO and H_2 is represented by the following:

$$CH_4\ (g) + O^{2-}\ (surf/latt) \rightarrow CO(g) + 2H_2(g) + \square$$

whereas the consumption of two oxygen species accounts for the formation of CO_2 and H_2:

$$CH_4\ (g) + 2O^{2-}\ (surf/latt) \rightarrow CO_2\ (g) + 2H_2\ (g) + 2\square$$

Thus, consumption of exchangeable oxygen during CH_4 activation regenerates oxygen-deficient sites. Restoration of the storage function for the subsequent cycle can be represented functionally by the following:

$$\square + CO_2\text{-derived oxygen species} \rightleftharpoons \text{regenerated O-containing surface}$$

This restoration closes the storage–regeneration sequence and makes the surface available for the subsequent CO_2-SR cycle. These expressions represent simplified functional pathways; methane reforming, cracking and reactions involving carbonate-derived intermediates may occur concurrently. The idealized overall balance is represented by the following:

$$CO_2\ (g) + CH_4\ (g) \rightarrow 2CO\ (g) + 2H_2\ (g)$$

This equation represents the idealized net stoichiometry of the complete CO_2-SR cycle. It does not imply simultaneous exposure of the catalyst to gaseous CO_2 and CH_4 or a single

elementary reaction pathway, but rather the net result of the sequential and coupled storage, oxygen exchange and CH_4-assisted regeneration processes.

The proposed scheme should therefore be regarded as a functional representation of the coupling between CO_2 storage, oxygen exchange, and methane-assisted regeneration, rather than as a unique sequence of elementary reaction steps. The comparison indicates that the NiBaCe catalyst incorporates an additional Ce-associated redox domain relative to the NiBa reference; however, the present catalyst series does not allow the specific contribution of Ce to be fully decoupled from the concomitant changes in Ni/Ba/Ce composition. The mechanistic interpretation is therefore framed in terms of the experimentally observed catalyst architecture and redox response, rather than as evidence for a unique Ce-driven pathway.

From this perspective, CO_2-SR performance is governed not only by the individual capacity of each function, but also by their balance, accessibility, and dynamic coupling during cyclic operation. These three descriptors thus emerge as key catalyst design criteria for the development of trifunctional materials and the further advancement of CO_2-SR technology.

3. Materials and Methods

3.1. Catalyst Synthesis

NiBa and NiBaCe catalysts, with atomic nominal compositions of Ni/Ba=10/1 and Ni/Ba/Ce=3/1/5, respectively, were prepared by ultrasound-assisted coprecipitation, following the procedure previously reported for the unsupported Ni–M catalyst series [20]. $Ni(NO_3)_2{\cdot}6H_2O$ from Panreac Química S.L.U. (PanReac AppliChem, Barcelona, Spain) and $Ba(NO_3)_2$ from Sigma-Aldrich (Merck KGaA, St. Louis, MO, USA) were used as the Ni and Ba precursors, respectively, while $Ce(NO_3)_3{\cdot}6H_2O$ from Sigma-Aldrich was additionally used as the Ce precursor for the NiBaCe formulation. Colloidal silica (LUDOX HS-40) from Sigma-Aldrich was added in an amount corresponding to 3 wt.% SiO_2 in the final material, acting as a nucleating and textural promoter.

The precursor mixture was sonicated and subsequently maintained under stirring overnight at 30 °C. Aqueous ammonia was then added dropwise until a pH of 9–10 was reached to induce coprecipitation. The resulting precipitate was aged and thoroughly washed to remove residual soluble species, and subsequently dried in static air at 90 °C for 12 h. Finally, the dried material was calcined in air at 800 °C for 4 h using a heating rate of 5 °C·min^{-1}.

3.2. Textural and Structural Characterization

Nitrogen adsorption–desorption isotherms of the calcined catalysts were recorded at −196 °C using a Micromeritics ASAP 2020 analyzer (Norcross, GA, USA). Prior to the measurements, the samples were degassed under vacuum (10^{-3} Pa) at 80 °C. The specific surface area (A_{BET}) was calculated using the Brunauer–Emmett–Teller (BET) method. The total pore volume (V_p) was estimated from the amount of N_2 adsorbed at high relative pressure, whereas the average pore diameter (d_p) was obtained from the adsorption branch of the isotherm using the Barrett–Joyner–Halenda (BJH) method.

X-ray diffraction (XRD) patterns of the calcined catalysts were recorded using a PANalytical X'Pert Pro MPD (PANalytical, Malvern, UK) diffractometer equipped with Cu Kα_1 radiation (λ = 1.5406 Å) and a Ge(111) primary monochromator. Diffraction patterns were collected over a 2θ range of 10–80°. Crystalline phases were identified by comparison with reference patterns from the International Centre for Diffraction Data (ICDD). Unit-cell parameters were determined by Rietveld refinement. The average crystallite size was estimated from the broadening of the diffraction peaks using the Williamson–Hall

(W–H) method, which considers both crystallite size and lattice microstrain contributions to peak broadening.

3.3. Surface Chemical Characterization

X-ray photoelectron spectroscopy (XPS) measurements were carried out under ultra-high vacuum on a Physical Electronics (PHI) 5700 spectrometer fitted with a Mg/Al X-ray source (PHI 04-548) and a hemispherical electron analyzer (PHI 10-360 Precision Energy Analyzer with multichannel detector, Chanhassen, MN, USA). Al Kα radiation (1486.6 eV; 100 W, 20 kV, 100 µm beam) was used together with a dual-beam charge neutralizer. Binding energies were referenced to the C 1s signal of adventitious carbon at 284.8 eV, with an accuracy of ±0.2 eV, and spectra were deconvoluted using mixed Gaussian–Lorentzian functions (60–80%). XPS analysis was used to determine the surface chemical states and relative contributions of Ni, Ba, Ce and O species, with particular attention to the Ce^{3+}/Ce^{4+} distribution and the different contributions to the O 1s region.

CO_2 temperature-programmed desorption (CO_2-TPD) experiments were performed using a Micromeritics AutoChem III instrument (Micromeritics Instrument Corp., Norcross, GA, USA) to evaluate the CO_2 uptake and the thermal stability of adsorbed CO_2-derived species. Approximately 15 mg of catalyst was pretreated under He (50 mL·min^{-1}) by heating from room temperature to 800 °C at 10 °C·min^{-1} and holding at 800 °C for 1 h. The sample was subsequently cooled under He to 60 °C and exposed to pure CO_2 (50 mL·min^{-1}) for 10 min to allow for CO_2 adsorption. After CO_2 exposure, the sample was purged with He (50 mL·min^{-1}) to remove gas-phase and weakly adsorbed CO_2. The temperature was then increased from 60 to 800 °C at a heating rate of 30 °C·min^{-1} under He. During the temperature-programmed step, the evolution of CO_2 and CO was continuously monitored, allowing both molecular CO_2 desorption and the formation of CO from adsorbed CO_2-derived species to be followed. The integrated CO_2 response was used to estimate the amount of CO_2 released during the temperature-programmed experiment, whereas the temperature distribution of the CO_2 and CO signals was used to compare the thermal stability and transformation of the adsorbed CO_2-derived species.

Hydrogen temperature-programmed reduction (H_2-TPR) experiments were carried out using the Micromeritics AutoChem III system equipped with a thermal conductivity detector (TCD) to evaluate the reducibility of the catalysts and the temperature distribution of their reducible species. Approximately 15 mg of catalyst was heated from room temperature to 800 °C at 10 °C·min^{-1} under a 10 vol.% H_2/Ar mixture flowing at 50 mL·min^{-1}. The H_2 consumption profile was continuously recorded as a function of temperature. The position and relative intensity of the reduction features were used to compare the reduction behavior of the different reducible environments present in NiBa and NiBaCe.

3.4. Oxygen Pulse Experiments

The transient oxygen uptake and reoxidation behavior of the NiBa and NiBaCe catalysts was investigated by using the Transient Response Method (TRM), using a U-shaped quartz fixed-bed reactor connected to a QMS 200 mass spectrometer (Pfeiffer Vacuum Prisma, Asslar, Germany). Prior to the experiment, each catalyst was reduced in situ under an H_2/He stream at 600 °C for 1 h. The reduced catalyst was subsequently exposed to successive 250 µL O_2 pulses, each followed by a 6 min He purge, while the O_2, CO, CO_2 and H_2O signals were continuously monitored at the reactor outlet. The pulse sequence was continued until the O_2 response reached a stable plateau, corresponding to complete O_2 breakthrough under the experimental conditions. All experiments were performed isothermally at 600 °C and atmospheric pressure.

The evolution of the O_2 response was evaluated relative to the final stable signal obtained after complete breakthrough. Two characteristic times were used to compare the transient behavior of the catalysts: the breakthrough time (t_b) and the half-response time ($t_{1/2}$). The breakthrough time, t_b, was estimated as the elapsed time at which O_2 became persistently detectable at the reactor outlet, indicating the onset of breakthrough. The half-response time, $t_{1/2}$, was determined as the time required for the O_2 response to reach 50% of its final stable value. Because O_2 was supplied as discrete pulses, these parameters represent characteristic times of the overall transient reoxidation process rather than intrinsic kinetic constants. The experimental procedure and transient descriptors were based on the methodology previously applied to this catalyst series [45].

3.5. Catalytic Performance Under CO_2-SR Cyclic Conditions

The cyclic CO_2 storage and CH_4 regeneration behavior of the NiBa and NiBaCe catalysts was evaluated in a Microactivity Effi reactor (PID Eng&Tech S.L., Madrid, Spain) using 100 mg of catalyst and a total flow rate of 100 mL·min^{-1} (GHSV = 20,000 h^{-1}). Each cycle consisted of a 10 min CO_2 storage pulse, followed by a 10 min He purge, a 10 min CH_4 regeneration pulse and a further 10 min He purge, resulting in a total cycle duration of 40 min. CO_2 and CH_4 were independently fed at 30,000 ppm in He. The He purge steps prevented direct mixing between the CO_2 and CH_4 streams and allowed the storage and regeneration stages to be analyzed separately. All experiments were conducted isothermally at 600 °C and atmospheric pressure.

Prior to the cyclic experiments, each catalyst was activated in situ under a 30,000 ppm H_2/He stream at 600 °C for 1 h. The reactor outlet composition was continuously monitored using a GAM 200 mass spectrometer (InProcess Instruments, Bremen, Germany) and a MultiGas 2030 FTIR gas analyzer (MKS Instruments, Andover, MA, USA). The amount of CO_2 retained during the storage step and the amount of CH_4 converted during the regeneration step were determined by numerical integration of the corresponding calibrated outlet concentration profiles relative to a blank experiment performed under identical conditions in the absence of catalyst.

For each CO_2-SR cycle, the outlet concentration profiles corresponding to the regeneration period were integrated to evaluate the evolution of the product distribution. The CO_2/CO ratio was calculated from the integrated CO_2 and CO concentration profiles, whereas the H_2/CO_x ratio was calculated from the integrated H_2 concentration profile relative to the sum of the integrated CO and CO_2 profiles.

4. Conclusions

This work contributes to the development of CO_2-SR as a cyclic CO_2 capture-and-conversion technology through the design of trifunctional catalysts integrating CO_2 storage, oxygen exchange and CH_4-assisted regeneration. The unsupported NiBaCe system was investigated in relation to the NiBa reference to assess how the introduction of Ce modifies the coupling between these functions. The combined characterization results show that NiBaCe exhibits higher CO_2 uptake, transformation of CO_2-derived species at lower temperature and a more readily reducible redox population.

Transient O_2 pulse experiments reveal distinct reoxidation behaviors for the two catalysts: NiBa exhibits prolonged O_2 consumption, whereas NiBaCe reaches its reoxidized state over a substantially shorter timescale. Under consecutive CO_2-SR cycles at 600 °C, both catalysts couple CO_2 storage with CH_4-assisted regeneration, while NiBaCe exhibits smaller cycle-to-cycle variations and a different product distribution. These results support a trifunctional architecture in which Ba-containing domains primarily provide CO_2 storage, Ni-containing sites promote CH_4 activation and regeneration, and Ce-

containing environments contribute to oxygen buffering and exchange within the interfacial redox network.

The modification of the model catalyst's composition therefore extends beyond changes in CO_2 uptake or reducibility, modifying the coupling between the storage, redox and regeneration functions of the catalyst. CO_2-SR performance consequently depends on the balance, accessibility and dynamic interaction of these functions rather than on their individual maximization. These features emerge as key design criteria for the development of trifunctional catalysts for CO_2-SR.

Author Contributions: S.E.-M.: Data curation, Investigation, Methodology, Writing—original draft. S.M.-R.: Data curation, Investigation, Methodology, Visualization. D.G.-G.: Investigation, Visualization. M.C.-R.: Conceptualization, Data curation, Formal analysis, Investigation, Methodology, Supervision, Validation, Writing—review and editing. C.H.: Conceptualization, Formal analysis, Funding acquisition, Investigation, Project administration, Writing—original draft, Writing—review and editing. M.Á.L.: Conceptualization, Formal analysis, Funding acquisition, Investigation, Project administration, Supervision, Writing—review and editing. L.J.A.: Conceptualization, Data curation, Formal analysis, Investigation, Methodology, Supervision, Validation, Writing—review and editing. All authors have read and agreed to the published version of the manuscript.:

Funding: This research was funded by the Spanish Ministry of Science, Innovation and Universities through projects PID2021-124098OB-I00 and PID2024-160658OB-I00.

Data Availability Statement: Data will be available on request.

Acknowledgments: The authors acknowledge the financial support from the Spanish Ministry of Science, Innovation and Universities (PID2021-124098OB-I00 and PID2024-160658OB-I00). SEM acknowledges the research fellowship provided by the University of Malaga.

Conflicts of Interest: The authors declare no conflicts of interest. The funders had no role in the design of the study; in the collection, analyses, or interpretation of data; in the writing of the manuscript; or in the decision to publish the results.

References

1. Sun, S.; Sun, H.; Williams, P.T.; Wu, C. Recent Advances in Integrated CO_2 Capture and Utilization: A Review. *Sustain. Energy Fuels* **2021**, *5*, 4546–4559. [CrossRef]
2. Ning, H.; Li, Y.; Zhang, C. Recent Progress in the Integration of CO_2 Capture and Utilization. *Molecules* **2023**, *28*, 4500. [CrossRef] [PubMed]
3. Zhang, Y.; Zhao, S.; Li, L.; Feng, J.; Li, K.; Huang, Z.; Lin, H. Integrated CO_2 Capture and Utilization: A Review of the Synergistic Effects of Dual Function Materials. *Catal. Sci. Technol.* **2024**, *14*, 790–819. [CrossRef]
4. Sun, H.; Sun, S.; Liu, T.; Zeng, J.; Wang, Y.; Yan, Z.; Wu, C. Integrated CO_2 Capture and Utilization: Selection, Matching, and Interactions between Adsorption and Catalytic Sites. *ACS Catal.* **2024**, *14*, 15572–15589. [CrossRef]
5. Asgari, M.; Iliuta, M.C. Highly Selective and Stable Cu-Based Dual-Function Materials for Integrated CO_2 Capture and in-Situ Conversion to CO. *Chem. Eng. J.* **2025**, *515*, 163366. [CrossRef]
6. Han, R.; Wang, Y.; Wei, L.; Peng, M.; Li, Z.; Liu, C.; Liu, Q. Integrated CO_2 Capture and Conversion by Cu/CaO Dual Function Materials: Effect of in-Situ Conversion on the Sintering of CaO and Its CO_2 Capture Performance. *Carbon Capture Sci. Technol.* **2024**, *12*, 100220. [CrossRef]
7. Duyar, M.S.; Treviño, M.A.A.; Farrauto, R.J. Dual Function Materials for CO_2 Capture and Conversion Using Renewable H_2. *Appl. Catal. B Environ.* **2015**, *168–169*, 370–376. [CrossRef]
8. Dan, M.; Mihet, M.; Borodi, G.; Lazar, M.D. Combined Steam and Dry Reforming of Methane for Syngas Production from Biogas Using Bimodal Pore Catalysts. *Catal. Today* **2021**, *366*, 87–96. [CrossRef]
9. Hossain, S.S.; Ayodele, B.V. Towards a Sustainable Hydrogen-Rich Syngas Production by Methane Dry Reforming: Advances in Catalyst Synthesis and Optimization Strategies. *Fuel* **2026**, *403*, 136132. [CrossRef]
10. Sun, S.; Zhang, Y.; Li, C.; Wang, Y.; Zhang, C.; Zhao, X.; Sun, H.; Wu, C. Upgrading CO_2 from Simulated Power Plant Flue Gas via Integrated CO_2 Capture and Dry Reforming of Methane Using Ni-CaO. *Sep. Purif. Technol.* **2023**, *308*, 122956. [CrossRef]
11. Zhang, L.; Zhou, Y.; Cui, H.; Cheng, Z.; Zhou, Z. Performance Enhancement of Ni/CaO-Al_2O_3 Dual-Function Materials for Integrated CO_2 Capture and Conversion via Dry Reforming of Methane. *Chem. Eng. Sci.* **2026**, *320*, 122635. [CrossRef]

12. Jo, S.; Gilliard-AbdulAziz, K.L. Self-Regenerative Ni-Doped $CaTiO_3$/CaO for Integrated CO_2 Capture and Dry Reforming of Methane. *Small* **2024**, *20*, 2401156. [CrossRef] [PubMed]
13. Niedbalka, D.; Marinis, G.A.; McKenna, M.; Krödel, M.; Abdala, P.M.; Donat, F.; Müller, C.R. Bifunctional MgO-Stabilized CaO Microspheres for Integrated CO2 Capture and Dry Reforming of Methane. *Carbon Capture Sci. Technol.* **2026**, *20*, 100664. [CrossRef]
14. Rostrup-Nielsen, J.R.; Sehested, J.; Noerskov, J.K. Hydrogen and Synthesis Gas by Steam- and CO_2 Reforming. *ChemInform* **2003**, *34*. [CrossRef]
15. Epling, W.S.; Peden, C.H.F.; Szanyi, J. Carbonate Formation and Stability on a Pt/BaO/γ-Al_2 O_3 NO_X Storage/Reduction Catalyst. *J. Phys. Chem. C* **2008**, *112*, 10952–10959. [CrossRef]
16. Li, C.; Gong, X.; Zhang, H.; Zhang, Y.; Yang, M.; Chen, B. CO_2 Capture Performance of CaO-Based Sorbent Modified with Torrefaction Condensate during Calcium Looping Cycles. *Chem. Eng. J.* **2023**, *469*, 144004. [CrossRef]
17. Wang, F.; Chen, S.; Chen, S.; Yuan, P.; Duan, L.; Xiang, W. CO_2 Capture and H_2 Production Performance of Calcium-Based Sorbent Doped with Iron and Cerium during Calcium Looping Cycle. *Process Saf. Environ. Prot.* **2024**, *188*, 1175–1190. [CrossRef]
18. Cortés-Reyes, M.; Herrera, C.; Larrubia, M.Á.; Alemany, L.J. Hybrid Technology for DeNOxing by LNT-SCR System for Efficient Diesel Emission Control: Influence of Operation Parameters in H_2O + CO_2 Atmosphere. *Catalysts* **2020**, *10*, 228. [CrossRef]
19. Castoldi, L.; Lietti, L.; Forzatti, P.; Morandi, S.; Ghiotti, G.; Vindigni, F. The NO_x Storage-Reduction on PtK/Al_2O_3 Lean NO_x Trap Catalyst. *J. Catal.* **2010**, *276*, 335–350. [CrossRef]
20. Essounani-Mérida, S.; Molina-Ramírez, S.; Cortés-Reyes, M.; Herrera, C.; Larrubia, M.Á.; Alemany, L.J. Influence of Second Metal Incorporation on Nickel-Based Unsupported Catalysts for CO_2 Reduction (CO_2-SR) Technology. *Results Eng.* **2025**, *26*, 104921. [CrossRef]
21. Essounani-Mérida, S.; Molina-Ramírez, S.; Cortés-Reyes, M.; Herrera, C.; Finocchio, E.; Larrubia, M.Á.; Alemany, L.J. Design of Unsupported Ni–Ba Catalysts for the CO_2 Storage-Regeneration (CO_2-SR) Process: Role of Ni/Ba Surface Domains and Rh Promotion. *Catalysts* **2026**, *16*, 376. [CrossRef]
22. Molina-Ramírez, S.; Peltzer, D.; Cortés-Reyes, M.; Herrera, C.; Larrubia, M.A.; Cornaglia, L.; Alemany, L.J. CO_2-SR Technology Using NiBa Unsupported Catalyst. Isotopic Study of Cyclic Process of CO_2 Storage and in Situ Regeneration with CH_4. *Fuel* **2023**, *341*, 127690. [CrossRef]
23. Trovarelli, A.; Fornasiero, P. *Catalysis by Ceria and Related Materials*, 2nd ed.; World Scientific (Firm), Ed.; Catalytic science series; World Scientific Pub. Co.: Singapore, 2013.
24. Montini, T.; Melchionna, M.; Monai, M.; Fornasiero, P. Fundamentals and Catalytic Applications of CeO_2 -Based Materials. *Chem. Rev.* **2016**, *116*, 5987–6041. [CrossRef] [PubMed]
25. Wang, D.; Liu, J.; Che, Y.; Yang, H.; Li, B.; Su, T.; Zhang, J. Steam-Assisted Dry Reforming of Methane over a Ce-Doped Ni/Calcium Aluminate Catalyst Enabling Stable Syngas Production. *Fuel* **2026**, *418*, 138766. [CrossRef]
26. Ahn, S.-Y.; Jang, W.-J.; Shim, J.-O.; Jeon, B.-H.; Roh, H.-S. CeO_2 -Based Oxygen Storage Capacity Materials in Environmental and Energy Catalysis for Carbon Neutrality: Extended Application and Key Catalytic Properties. *Catal. Rev.* **2024**, *66*, 1316–1399. [CrossRef]
27. Pu, Z.; Liu, Q.; Chen, C.; Wang, F. Promoting Surface Lattice Oxygen and Oxygen Vacancy of CeO_2 for Photothermal Methane Dry Reforming over Ni/CeO_2 Catalysts. *Chem. Eng. J.* **2024**, *497*, 154861. [CrossRef]
28. Han, K.; Yu, W.; Xu, L.; Deng, Z.; Yu, H.; Wang, F. Reducing Carbon Deposition and Enhancing Reaction Stability by Ceria for Methane Dry Reforming over Ni@SiO_2@CeO_2 Catalyst. *Fuel* **2021**, *291*, 120182. [CrossRef]
29. Li, C.; Zhang, M.; Gao, Q.; Wang, J.; Zhang, J.; Zhang, Q.; Han, Y. A Review on the Mechanisms of Carbon Deposition and Removal and Strategies for Resolving Carbon Deposition-Induced Deactivation in Dry Reforming of Methane. *Mol. Catal.* **2026**, *596*, 115920. [CrossRef]
30. Pu, T.; Chen, J.; Tu, W.; Xu, J.; Han, Y.-F.; Wachs, I.E.; Zhu, M. Dependency of CO_2 Methanation on the Strong Metal-Support Interaction for Supported Ni/CeO_2 Catalysts. *J. Catal.* **2022**, *413*, 821–828. [CrossRef]
31. Wang, T.; Tang, R.; Li, Z. Enhanced CO_2 Methanation Activity over Ni/CeO_2 Catalyst by Adjusting Metal-Support Interactions. *Mol. Catal.* **2024**, *558*, 114034. [CrossRef]
32. Löfberg, A.; Guerrero-Caballero, J.; Kane, T.; Rubbens, A.; Jalowiecki-Duhamel, L. Ni/CeO_2 Based Catalysts as Oxygen Vectors for the Chemical Looping Dry Reforming of Methane for Syngas Production. *Appl. Catal. B Environ.* **2017**, *212*, 159–174. [CrossRef]
33. Zhang, Q.; He, F.; Hu, Q.; Yang, G.; Chen, Y.; Yang, H.; Yang, Y. Efficient Ni/$CaCeO_x$ Dual-Functional Materials for Integrated CO_2 Capture and Dry Reforming of CH_4 for Syngas Production. *Chem. Eng. J.* **2026**, *542*, 177290. [CrossRef]
34. Zhang, X.; Liu, X.; Guo, J.; Guo, Y.; Qi, L.; Yu, Y.; Zhang, Z.; Zhou, Y.; Huang, P.; Wang, G.; et al. Unveiling the Role of Adsorbent–Catalyst Proximity in Integrated CO_2 Capture and Dry Reforming of Methane over Ni-CaO/CeO_2 Systems. *Ind. Eng. Chem. Res.* **2026**, *65*, 13671–13688. [CrossRef]
35. Idriss, H. On the Wrong Assignment of the XPS O1s Signal at 531–532 eV Attributed to Oxygen Vacancies in Photo- and Electro-Catalysts for Water Splitting and Other Materials Applications. *Surf. Sci.* **2021**, *712*, 121894. [CrossRef]

36. Easton, C.D.; Morgan, D.J. Critical Examination of the Use of X-Ray Photoelectron Spectroscopy (XPS) O 1s to Characterize Oxygen Vacancies in Catalytic Materials and Beyond. *J. Vac. Sci. Technol. A* **2025**, *43*, 053205. [CrossRef]
37. Romeo, M.; Bak, K.; El Fallah, J.; Le Normand, F.; Hilaire, L. XPS Study of the Reduction of Cerium Dioxide. *Surf. Interface Anal.* **1993**, *20*, 508–512. [CrossRef]
38. Paparazzo, E. Use and Mis-Use of X-Ray Photoemission Spectroscopy Ce3d Spectra of Ce_2 O_3 and CeO_2. *J. Phys. Condens. Matter* **2018**, *30*, 343003. [CrossRef] [PubMed]
39. Thakur, V.; Gautam, S.; Rajput, P.; Jee, H.-G.; Chakraverty, S.; Gupta, M.; Chae, K.H.; Hwang, C.-C. Electronic Structural Investigation of Ni-Doped CeO_{2-y} for Catalytic Hydrogen Production: Exsitu XRD, XAS, and XPS Study. *Int. J. Hydrogen Energy* **2025**, *158*, 150258. [CrossRef]
40. Morgan, D.J. Photoelectron Spectroscopy of Ceria: Reduction, Quantification and the Myth of the Vacancy Peak in XPS Analysis. *Surf. Interface Anal.* **2023**, *55*, 845–850. [CrossRef]
41. Wang, J.; Mueller, D.N.; Crumlin, E.J. Recommended Strategies for Quantifying Oxygen Vacancies with X-Ray Photoelectron Spectroscopy. *J. Eur. Ceram. Soc.* **2024**, *44*, 116709. [CrossRef]
42. Luisetto, I.; Tuti, S.; Romano, C.; Boaro, M.; Di Bartolomeo, E.; Kesavan, J.K.; Kumar, S.S.; Selvakumar, K. Dry Reforming of Methane over Ni Supported on Doped CeO_2: New Insight on the Role of Dopants for CO_2 Activation. *J. CO_2 Util.* **2019**, *30*, 63–78. [CrossRef]
43. Giordano, F.; Trovarelli, A.; De Leitenburg, C.; Giona, M. A Model for the Temperature-Programmed Reduction of Low and High Surface Area Ceria. *J. Catal.* **2000**, *193*, 273–282. [CrossRef]
44. Feng, M.; Zhang, T.; Xiao, Z.; Zhang, J.; Zhang, X.; Li, G. Al Doped Ceria Supported Ni for Efficient Hydrogen Production via Methane Steam Reforming: Enhanced Ni Dispersion and Oxygen Vacancies. *Fuel* **2027**, *429*, 140827. [CrossRef]
45. Essounani-Mérida, S.; Molina-Ramírez, S.; Cortés-Reyes, M.; Herrera, C.; Ángeles Larrubia, M.; Finocchio, E.; Alemany, L.J. Oxygen Mobility and Redox Reversibility as Key Descriptors of CO_2 Storage and in Situ Regeneration: Insights from Unsupported NiBa and NiK Bifunctional Catalysts. *J. CO_2 Util.* **2026**, *112*, 103564. [CrossRef]

Disclaimer/Publisher's Note: The statements, opinions and data contained in all publications are solely those of the individual author(s) and contributor(s) and not of MDPI and/or the editor(s). MDPI and/or the editor(s) disclaim responsibility for any injury to people or property resulting from any ideas, methods, instructions or products referred to in the content.